Sublattice Dependence and Gate Tunability of Midgap and Resonant States Induced by Native Dopants in Bernal-Stacked Bilayer Graphene

Frédéric Joucken,[1,2,*] Cristina Bena,[3] Zhehao Ge,[1] Eberth Arturo Quezada-Lopez,[1] François Ducastelle,[4] Takashi Tanagushi,[5] Kenji Watanabe,[6] and Jairo Velasco, Jr.[1,†]

[1]*Department of Physics, University of California, Santa Cruz, California 95064, USA*
[2]*Department of Physics, Box 871504, Arizona State University, Tempe, Arizona 85287, USA*
[3]*Institut de Physique Théorique, Université Paris Saclay, CEA CNRS, Orme des Merisiers, 91190 Gif-sur-Yvette Cedex, France*
[4]*Laboratoire d'Etude des Microstructures, ONERA-CNRS, UMR104, Université Paris-Saclay, B.P. 72, 92322 Châtillon Cedex, France*
[5]*International Center for Materials Nanoarchitectonics, National Institute for Materials Science, 1-1 Namiki, Tsukuba 305-0044, Japan*
[6]*Research Center for Functional Materials, National Institute for Materials Science, 1-1 Namiki, Tsukuba 305-0044, Japan*

(Received 28 April 2021; accepted 8 July 2021; published 31 August 2021)

The properties of semiconductors can be crucially impacted by midgap states induced by dopants, which can be native or intentionally incorporated in the crystal lattice. For Bernal-stacked bilayer graphene (BLG), which has a tunable band gap, the existence of midgap states induced by dopants or adatoms has been investigated theoretically and observed indirectly in electron transport experiments. Here, we characterize BLG midgap states in real space, with atomic-scale resolution with scanning tunneling microscopy and spectroscopy. We show that the midgap states in BLG—for which we demonstrate gate tunability—appear when the dopant is hosted on the nondimer sublattice sites. We further evidence the presence of narrow resonances at the onset of the high-energy bands (valence or conduction, depending on the dopant type) when the dopants lie on the dimer sublattice sites. Our results are supported by tight-binding calculations that agree remarkably well with the experimental findings.

DOI: 10.1103/PhysRevLett.127.106401

Midgap states induced by dopants or defects have historically been of central importance in semiconductor physics because of their key role in the electronic transport properties and on the light absorption or emission of materials [1,2]. This is also the case for two-dimensional van der Waals semiconductors, which have attracted enormous attention in the past decade. Dopant- and defect-induced midgap states have been shown to play a central role, e.g., in the exciton formation and dynamics in two-dimensional (2D) transition metal dichalcogenides (TMDs) [3–7]. Several reports have also established the drastic influence of these midgap states on the transport properties of 2D semiconducting TMDs [8–10]. Scanning tunneling microscopy (STM) investigations conducted on doped 2D semiconducting TMDs have revealed their spatial configuration and their electronic structure at the atomic scale [11–15]. Bernal-stacked bilayer graphene (BLG) is also a semiconducting 2D material, particularly known for its unique tunable band gap [16–18]. This property makes BLG especially promising for quantum information technology, as it allows designing gate-defined confinement regions such as constrictions [19] or quantum dots [20–25]. Such devices require a pristine electronic response free of impurity-induced midgap states to maintain quantum coherence [26].

Impurity-induced midgap states in BLG have been investigated theoretically [27–31]. The transport properties of biased doped BLG were studied by Ferreira *et al.* [32] and Yuan, De Raedt, and Katsnelson [33], who predicted a plateau in conductivity around the charge neutrality point. This plateau and its dependence on the vertical electric field were later observed experimentally with transport measurements by Stabile *et al.* [34]. The problems of localization [30] and the Kondo effect [29] have also been investigated theoretically. More recently, the sublattice dependence of the dopants was indirectly evidenced by transport in an ultrahigh vacuum environment by Katoch *et al.* [35]. To date, however, no local probe characterization of impurity states in biased BLG has been reported. Such characterization offers unique information on the modification of the local density of states (LDOS) induced by the dopants.

We report in this Letter atomic-scale characterization of dopant-induced midgap states in BLG. With data obtained on dopants with both positive and negative potential signs, we show that the dopants induce a midgap state only when sitting on the nondimer sublattice sites. We demonstrate the tunability of the midgap states with the electrostatic back gate. We also demonstrate the existence of narrow resonant states located at the onset of the high-energy bands when the dopant lies on the dimer sublattice sites. Although

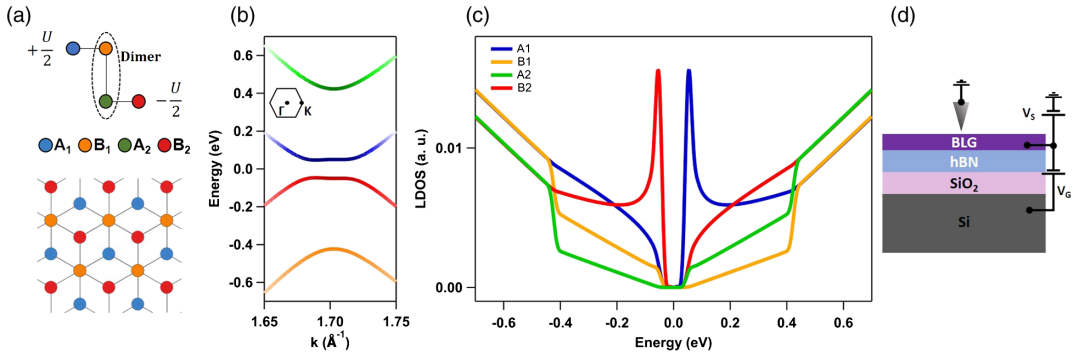

FIG. 1. Bernal-stacked bilayer graphene (BLG) lattice, band structure, and local density of states (LDOS). (a) Lattice structure of BLG. (b) Band structure of BLG, around the K point. (c) Local density of states on each sublattice site for $U = +100$ meV. The color code used in (b) is indicative of the LDOS on each sublattice site. (d) Schematics of the back-gated BLG device investigated by scanning tunneling microscopy in this work.

inaccessible in transport experiments, these high energy states will likely influence the optical properties of BLG. Our findings are supported by tight-binding-based simulations agreeing remarkably well with the experiments.

The lattice structure of BLG and our convention for sublattice labeling are shown in Fig. 1(a). As McCann and Koshino did, we refer to the A_2 and B_1 sublattice sites as dimer sites because of the strong coupling between the orbitals of atoms located on them [18]. By the same token, we refer to A_2 and B_1 as nondimer sites. Figure 1(b) shows the band structure of BLG around the K point with an interlayer potential of $U = 100$ meV [see Fig. 1(a) for the polarity; other tight-binding parameters are $\gamma_0 = 3.3$ eV, $\gamma_1 = 0.42$ eV, and $\gamma_3 = -0.3$ eV [36] following the convention from Ref. [18]]. Note that for simplicity we ignore the difference between the interlayer potential (U) and the gap (U_G), because it is negligible in the range we consider here (<90 meV). The LDOS on each sublattice is shown in Fig. 1(c). The color of each band in Fig. 1(b) reflects the distribution of the LDOS on each sublattice, as seen in Fig. 1(c). The LDOS plotted in Fig. 1(c) show the strong lattice dependence of the electronic density in gapped BLG. The prominent van Hove singularity (vHs; discontinuity of the density of states and divergence of its Hilbert transform) at the gap edges (low energy) are spatially located around the nondimer sites, whereas the weaker vHs corresponding to the onset of the higher-energy bands can be associated with the dimer sites.

The sample we have investigated consists in a BLG on hexagonal boron nitride (BLG/hBN) heterostructure deposited on SiO_2/Si (see Supplemental Material, Sec. 1 [37], which includes Refs. [24,38–40], for details on sample fabrication). In our STM experiments, the tip is grounded, and a bias is applied to the sample (V_S), while the silicon substrate serves as an electrostatic gate (V_G); a schematic of the device is shown in Fig. 1(d). As we have recently reported [41], native defects and dopants are found in these samples. It is challenging to find and characterize these dopants with STM, because, although their effects are striking [41], their concentration is extremely low ($\sim 1 - 2 \times 10^9$ cm^{-2}). However, an advantage of having such a low concentration of defects and dopants is that interactions between them [42,43] are negligible, simplifying somewhat the comparison between experiments and simulations.

We start by presenting the sublattice dependence of the dopant-induced localized states in gapped BLG (Fig. 2). Figures 2(a) and 2(b) show dI/dV_S spectra acquired atop the dopants shown in the STM topography images displayed in the respective insets (red crosshairs). The dotted gray spectra in Figs. 2(a) and 2(b) are reference spectra obtained ~3 nm away from the dopants. The spectra were obtained at $V_G = +30$ V, corresponding to $U_G = 64$ meV (see Supplemental Material, Sec. 2 [37], which includes Refs. [44–46], for details on the band gap determination). Superimposing atomic lattice schematics to the STM image (see Supplemental Material, Sec. 3 [37], which includes Ref. [47]) suggests that the dopant in Fig. 2(a) is located on the B_1 sublattice (dimer site), whereas the dopant in Fig. 2(b) is located on the A_1 sublattice (nondimer site). The spectra of Figs. 2(a) and 2(b) both display a broad state in the conduction band ($V_S \approx +0.75$ V) similar to what is observed atop a nitrogen dopant in monolayer graphene [48], indicating the dopant should be donorlike, with an attractive potential [49]. We refer to this state as the *broad resonance*.

The spectroscopic and the topographic STM signatures of the dopants shown in Figs. 2(a) and 2(b) are similar to the signatures of nitrogen dopants in monolayer graphene [48,50,51]. Also, the topographic STM signature of nitrogen dopant in BLG was shown to resemble closely the signature in monolayer graphene [52,53]. We thus identify the observed dopants as nitrogen. The spectra in Figs. 2(a) and 2(b) also display two very clear differences. The first difference is found close to the Fermi level ($V_S = 0$): A state is clearly visible for the dopant on the A_1 sublattice, while no state is seen for the dopant on the B_1 sublattice. It lies at the conduction band gap edge. We refer to it as the *midgap state* and associate it to the predictions made by earlier theoretical work [27,31], as we show below.

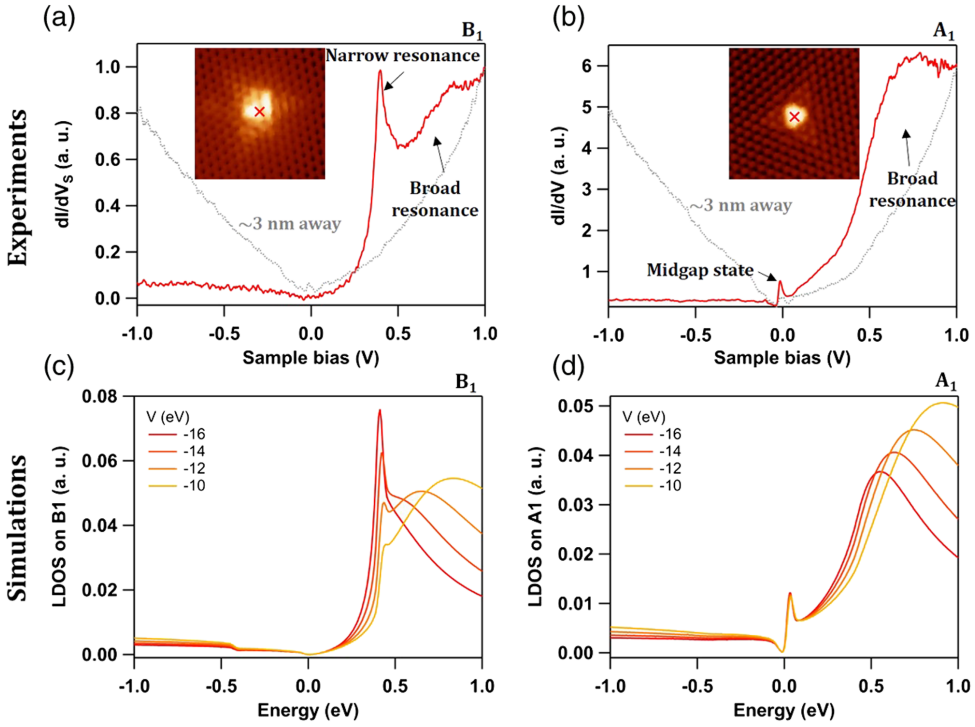

FIG. 2. Sublattice dependence of the spectroscopic signature of a nitrogen dopant in BLG. (a) Experimental dI/dV_S spectrum acquired atop a nitrogen dopant located on the B_1 sublattice. Inset: 3×3 nm^2 topographic STM image of the dopant; z scale is 0.14 nm, $V_S = +1$ V, $I = 0.5$ nA, and $V_G = +30$ V. (b) Experimental dI/dV_S spectrum acquired atop a nitrogen dopant located on the A_1 sublattice. Inset: 3×3 nm^2 topographic STM image of the dopant; z scale is 0.14 nm, $V_S = -0.3$ V, $I = 0.5$ nA, and $V_G = +30$ V. Data acquired at a gate voltage $V_G = +30$ V and setpoint $I = 0.5$ nA and $V_S = -1$ V. Spectra were acquired at the location indicated by the red crosshairs in the topographic image. In (a) and (b), the gray spectrum is a reference acquired in a pristine region, ~3 nm away from the dopant, with the same conditions, for comparison. (c) Simulated LDOS of a dopant located on the B_1 sublattice, modeled by the indicated on-site energy ($V = -10, -12, -14$, and -16 eV) (d) Simulated LDOS of a dopant located on the A_1 sublattice, modeled by the indicated on-site energy ($V = -10, -12, -14$, and -16 eV). The main features seen in (a) and (b) are well reproduced in (c) and (d).

(Note that, although the state lies at the edge of the gap, we follow the terminology of Nilsson and Castro Neto [27] and refer to it as the *midgap* state.) Another difference can be seen at $V_S \approx 0.40$ V, where a narrow peak in the spectrum can be seen only for the defect located on the B_1 sublattice, no such state being seen for the defect on A_1. We refer to this state as the *narrow resonance*. Importantly, these three states (midgap state and broad and narrow resonances) are well localized on the dopants, as they are not present ~3 nm away from the dopants [gray spectra in Figs. 2(a) and 2(b); we also present more spatially dependent spectra in Supplemental Material, Sec. 4]. Also, note that, in pristine regions, the sharp peak associated with the low-energy vHs, which would be expected to appear in the STS spectra [red and blue curves in Fig. 1(c)], turns out to be very weak. Finally, over the energy range that we have probed (± 1 eV), only a faint sublattice dependence is observed in the pristine regions [54]. We discuss this point in detail in Sec. 5 in Supplemental Material [37], which includes Ref. [54].

To clarify the origin of these states, we next compare our experimental data to tight-binding simulations. Figures 2(c) and 2(d) display computed LDOS on the B_1 and A_1 sublattices (respectively) for a dopant located on the B_1 and A_1 sublattices (respectively). The dopant is modeled by modifying the on-site energy at the specific sublattice position, and the results are shown for a range of on-site energy values (details on the calculations are given in Sec. 6 in Supplemental Material [37], which includes Refs. [55,56]). An excellent agreement between the simulated LDOS and the experimental dI/dV_S spectra can be seen. In both cases, the broad resonance in the conduction band is reproduced by the simulations, and the position in energy is comparable to experiment. Notably, the state next to the Fermi level is also well reproduced in the simulations. In addition, the narrow resonance at $\approx$0.40 eV for the B_1 case is well reproduced. Note that the position of the state in energy coincides with the onset of the high-energy band [Fig. 1(b)] and that simulations show that a dopant located on A_2 (the other dimer site) results in very similar LDOS to a dopant located on B_1 (peak in the LDOS also located in the conduction band; see Supplemental Material [37]). This narrow resonance located at the high-energy band onset can be expected because of the vHs associated with the dimer sites (B_1 and A_2 sublattices; see Fig. 1). As the midgap state (edge of the low-energy band) is produced by the dopant

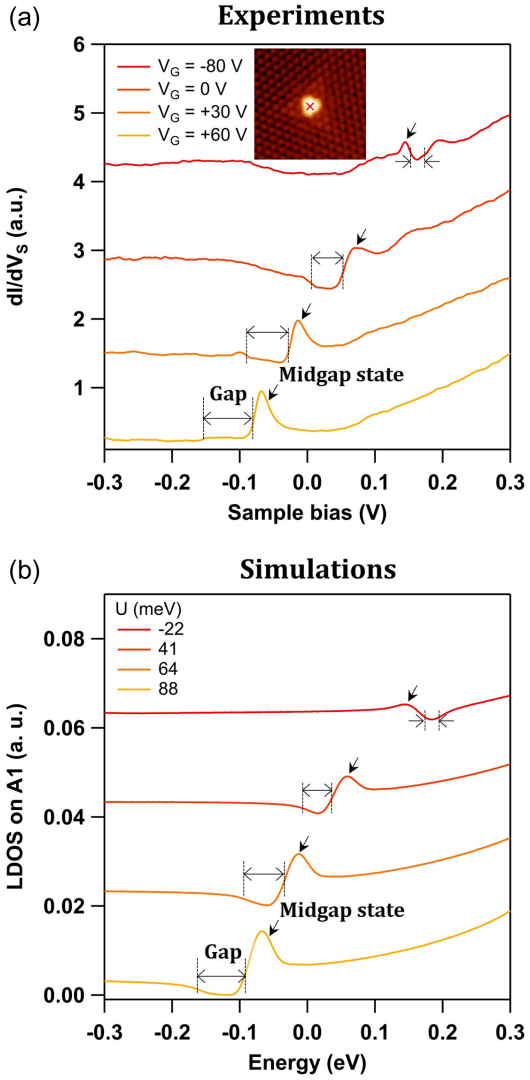

FIG. 3. Gate dependence of the midgap state associated to a nitrogen dopant in BLG. (a) Experimental dI/dV_S spectra obtained atop a nitrogen dopant located on the A_1 sublattice for various gate voltages. Inset: 3×3 nm^2 topographic STM image of the dopant; z scale is 0.14 nm, $V_S = -0.3$ V, $I = 0.5$ nA, and $V_G = +30$ V. The spectra were acquired at the position indicated by the red crosshair in the topographic image. (b) Simulated LDOS for the A_1 sublattice for a dopant modeled by an on-site energy $V = -12$ eV. In (a) and (b), the midgap state and the gap are indicated. For an unknown reason, the gap edge on the valence band side is not clearly visible for $V_G = +60$ V in (a). Curves in (a) and (b) are shifted vertically for clarity. The simulated LDOS are shifted manually in energy to match the position of the midgap state in the experiments.

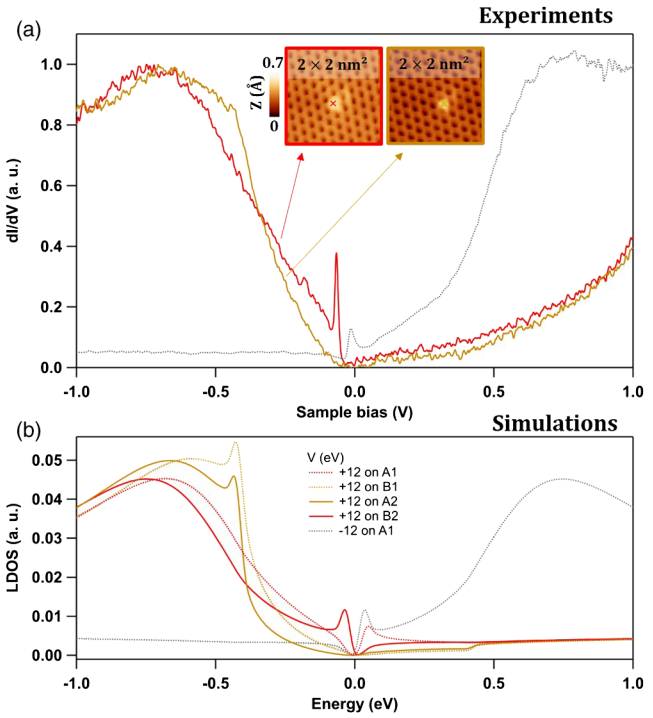

FIG. 4. Spectroscopic signature of dopants other than nitrogen in BLG. (a) Experimental dI/dV_S spectrum obtained atop the dopants shown in the inset ($I = 0.5$ nA; $V_S = -1$ V; $V_G = +30$ V). Crosses indicate the positions where the spectra were acquired. The correspondence between spectra and dopants is indicated by the arrows. The dotted gray curve is the experimental dI/dV_S spectrum obtained atop the nitrogen dopant located on the A_1 sublattice [Fig. 2(b)] shown here for comparison. (b) Simulated LDOS for a dopant modeled by an on-site potential $V = +12$ eV on all sublattice sites; the gray curve is the computed LDOS at A_1 for an on-site potential $V = -12$ eV on A_1, for comparison. The LDOS plotted is the LDOS at the dopant position.

lying on a nondimer site, a dopant lying on a dimer site can be expected to produce a resonant state located at the edge of the associated high-energy band [see Fig. 1(c)] [57].

We now explore the gate tunability of the observed midgap state. In Fig. 3(a), we present the gate-dependent STS data obtained atop the nitrogen dopant located on the A_1 sublattice [the same dopant as in Fig. 2(b)]. The simulated LDOS for the corresponding gap values (see Supplemental Material, Sec. 2 [37], for gap determination) is shown in Fig. 3(b), for an on-site potential $V = -12$ eV. The LDOS curves in Fig. 3(b) have been shifted vertically for clarity and horizontally to match the gate dependence observed experimentally [Fig. 3(a)]. The gap is indicated on the LDOS curves in Fig. 3(b), as well as in the experimental data in Fig. 3(a). The gap edge on the valence band side is not clearly resolved experimentally for $V_G = +60$ V in Fig. 3(a) (unknown reason). A very good agreement between the simulations and the experiment is evident. As the gate (and the gap) increases, the midgap state becomes more prominent, as can be intuitively expected, since the midgap state disappears when the gap closes [27,31]. Note also that we observe the midgap state very close to the conduction band edge. The separation between the midgap state and the band edge is not resolved within our experimental resolution, which we estimate at 15 meV (the amplitude of the lock-in excitation; see Sec. 1 in Supplemental Material [37]). This is in agreement with the values anticipated theoretically [27,31]. We must however note that, although the state seen experimentally in Fig. 3(a) can be unequivocally attributed to the

midgap state, the simulated LDOS curves for the pristine case (in the absence of a defect) display a similar shape as seen in Fig. 3(b), only with a less intense peak at the band edge (see Sec. 5 in Supplemental Material [37]). This peak corresponds to the low-energy vHs expected on A_1 (see Fig. 1). As already mentioned, the low-energy vHs peak in pristine regions turns out to be very weak in STS spectra [54].

In addition to the dopant that causes the midgap state discussed so far, we observed another type of dopant that also produces a broad resonance, but in the valence band. Figure 4(a) shows dI/dV_S spectra obtained atop the dopants whose STM topographic images are shown as insets. We also reproduce in Fig. 4(a) the experimental spectrum obtained atop the N dopant located on A_1 in light dotted gray [Fig. 2(b)], for convenient comparison. Both dopants display a broad resonance at $V_S \approx -0.75$ V. However, only the red curve displays a midgap state (narrow peak close to $V_S = 0$). Also, the gold curve shows a slight shoulder around $V_S = -0.4$ V.

To understand the origin of the states seen in our experiments [Fig. 4(a)], we show in Fig. 4(b) simulated LDOS for dopants modeled by an on-site potential $V = +12$ eV located on A_2, B_2, and B_1 (we also show the LDOS for $V = -12$ eV on A_1, for comparison). Because of the agreement between the red solid line curves in Figs. 4(a) and 4(b), we can confidently assign the red spectrum in Fig. 4(a) to a dopant located on the B_2 sublattice (nondimer site) with repulsive potential ($V = +12$ eV). For the other unknown dopant (gold curve), the situation is less straightforward, as both simulated LDOS for a dopant on the B_1 and the A_2 sublattices (dimer sites) with $V = +12$ eV reproduce the experimental dI/dV_S spectrum: The absence of a midgap state and the shoulder at the onset of the high-energy band ($V_S = -0.4$ V) are both observed. Note that $V_S = -0.4$ V corresponds to the onset of the high-energy band [similarly as the nitrogen dopant located on the B_1 sublattice; see Fig. 2(a)]. However, the similar low corrugation observed in the topographic STM images for both dopants indicates they both are most likely located in the bottom layer [52]. We, thus, tentatively assign the dopant corresponding to the gold curve to the sublattice A_2. Superimposed atomic lattice schematics on the STM images of the dopants are consistent with a dopant on B_2 (red) and A_2/B_1 (gold) (see Supplemental Material, Sec. 3 [37]).

It is difficult to identify the chemical nature of the dopants presented in Fig. 4(a), but a natural candidate is boron. The symmetry between nitrogen and boron for the broad resonance in the conduction or the valence band is expected from density functional calculations [52,58], and previous tunneling spectroscopy data on monolayer graphene suggested the presence of a broad resonance in the valence band [58–60]. Boron dopants are also expected to act as negatively charged defects (as opposed to nitrogen dopants which act as positively charged defects), and we show in Supplemental Material [37] (Sec. 7, which includes Refs. [61,62]) spatially dependent dI/dV_S spectra consistent with these polarities.

Finally, from Fig. 4(b), 2(c) and 2(d)], we summarize the rules for the position of the midgap state and the narrow and broad resonances. First, the sign of the on-site potential determines the position of the broad resonance: $V > 0$ ($V < 0$) gives a broad resonance in the valence (conduction) band. Second, the narrow resonance at the onset of the high-energy band is present if the dopant is on a dimer site (B_1 or A_2). Its position (valence or conduction band) does not depend on the sign of the electric field but only on the sign of the on-site potential. Its amplitude varies significantly with the on-site potential amplitude [see Fig. 2(c)]. Third, the midgap state is present if the dopant is located on a nondimer site (A_1 or B_2). It is flanking either the valence band or the conduction band edge, depending on which dimer site it is occupying and the orientation of the electric field. The dependence on the electric field is not illustrated in Fig. 4, but we show in Supplemental Material [37] (Sec. 8) complete results for the positions of the resonant states (broad and narrow) and the midgap state, as a function of the sublattice position, the on-site potential, and the electric field direction.

In conclusion, we have reported gate-dependent scanning tunneling spectroscopy results demonstrating the existence and the tunability of midgap states induced by native dopants in BLG. We have demonstrated that the midgap state appears when the dopant lies in the nondimer sites and shown how it can be tuned by the back gate voltage (perpendicular electric field). We have also shown that, when the dopant lies in the dimer sites, a narrow resonance appears at the edge of the high-energy bands. These higher-energy states, although inaccessible in transport experiments, should be observable (and tunable), for example, in optical absorption spectra [63], for samples with sufficient dopant concentration, in which case subbands are expected to appear [27,31]. Studying the evolution of these states with increasing dopant concentration achieved by intentional doping with angle-resolved photoemission spectroscopy and/or STM could reveal the development of these predicted gate-tunable bands.

J. V. J. acknowledges support from the National Science Foundation under Grant No. DMR-1753367 and the Army Research Office under Contract No. W911NF-17-1-0473. K. W. and T. T. acknowledge support from the Elemental Strategy Initiative conducted by the MEXT, Japan, Grant No. JPMXP0112101001 and JSPS KAKENHI Grant No. JP20H00354. F. J. carried out the STM measurements and carried out the tight-binding calculations. Z. G., E. A. Q.-L., and F. J. fabricated the graphene/hBN heterostructures. T. T. and K. W. synthesized the hBN crystals. F. J., F. D., and C. B. analyzed and interpreted the data. J. V. J. supervised the STM measurements and the sample fabrication. F. J. wrote the manuscript, with input from all coauthors.

*frederic.joucken@gmail.com
†jvelasc5@ucsc.edu

[1] F. Bassani, G. Iadonisi, and B. Preziosi, Electronic impurity levels in semiconductors, Rep. Prog. Phys. **37**, 1099 (1974).
[2] P. Van Mieghem, Theory of band tails in heavily doped semiconductors, Rev. Mod. Phys. **64**, 755 (1992).
[3] P. D. Cunningham, K. M. McCreary, A. T. Hanbicki, M. Currie, B. T. Jonker, and L. M. Hayden, Charge trapping and exciton dynamics in large-area CVD grown MoS_2, J. Phys. Chem. C **120**, 5819 (2016).
[4] V. Carozo, Y. Wang, K. Fujisawa, B. R. Carvalho, A. McCreary, S. Feng, Z. Lin, C. Zhou, N. Perea-López, A. L. Elías, B. Kabius, V. H. Crespi, and M. Terrones, Optical identification of sulfur vacancies: Bound excitons at the edges of monolayer tungsten disulfide, Sci. Adv. **3**, e1602813 (2017).
[5] K. Chen, R. Ghosh, X. Meng, A. Roy, J.-S. Kim, F. He, S. C. Mason, X. Xu, J.-F. Lin, D. Akinwande, S. K. Banerjee, and Y. Wang, Experimental evidence of exciton capture by mid-gap defects in CVD grown monolayer $MoSe_2$, npj 2D Mater. Appl. **1**, 15 (2017).
[6] K. Greben, S. Arora, M. G. Harats, and K. I. Bolotin, Intrinsic and extrinsic defect-related excitons in TMDCs., Nano Lett. **20**, 2544 (2020).
[7] S. V. Sivaram, A. T. Hanbicki, M. R. Rosenberger, G. G. Jernigan, H.-J. Chuang, K. M. McCreary, and B. T. Jonker, Spatially selective enhancement of photoluminescence in MoS_2 by exciton-mediated adsorption and defect passivation, ACS Appl. Mater. Interfaces **11**, 16147 (2019).
[8] S. Yuan, R. Roldán, M. I. Katsnelson, and F. Guinea, Effect of point defects on the optical and transport properties of MoS_2 and WS_2, Phys. Rev. B **90**, 041402(R) (2014).
[9] M. Ghorbani-Asl, A. N. Enyashin, A. Kuc, G. Seifert, and T. Heine, Defect-induced conductivity anisotropy in MoS_2 monolayers, Phys. Rev. B **88**, 245440 (2013).
[10] H. Qiu, T. Xu, Z. Wang, W. Ren, H. Nan, Z. Ni, Q. Chen, S. Yuan, F. Miao, F. Song, G. Long, Y. Shi, L. Sun, J. Wang, and X. Wang, Hopping transport through defect-induced localized states in molybdenum disulphide, Nat. Commun. **4**, 2642 (2013).
[11] S. Barja, S. Refaely-Abramson, B. Schuler, D. Y. Qiu, A. Pulkin, S. Wickenburg, H. Ryu, M. M. Ugeda, C. Kastl, C. Chen, C. Hwang, A. Schwartzberg, S. Aloni, S.-K. Mo, D. Frank Ogletree, M. F. Crommie, O. V. Yazyev, S. G. Louie, J. B. Neaton, and A. Weber-Bargioni, Identifying substitutional oxygen as a prolific point defect in monolayer transition metal dichalcogenides, Nat. Commun. **10**, 3382 (2019).
[12] B. Schuler, J.-H. Lee, C. Kastl, K. A. Cochrane, C. T. Chen, S. Refaely-Abramson, S. Yuan, E. van Veen, R. Roldán, N. J. Borys, R. J. Koch, S. Aloni, A. M. Schwartzberg, D. F. Ogletree, J. B. Neaton, and A. Weber-Bargioni, How substitutional point defects in two-dimensional WS2 induce charge localization, spin–orbit splitting, and strain, ACS Nano **13**, 10520 (2019).
[13] M. Aghajanian, B. Schuler, K. A. Cochrane, J.-H. Lee, C. Kastl, J. B. Neaton, A. Weber-Bargioni, A. A. Mostofi, and J. Lischner, Resonant and bound states of charged defects in two-dimensional semiconductors, Phys. Rev. B **101**, 81201(R) (2020).
[14] C.-P. Lu, G. Li, J. Mao, L.-M. Wang, and E. Y. Andrei, Bandgap, mid-gap states, and gating effects in MoS_2, Nano Lett. **14**, 4628 (2014).
[15] C. Zhang, C. Wang, F. Yang, J.-K. Huang, L.-J. Li, W. Yao, W. Ji, and C.-K. Shih, Engineering point-defect states in monolayer WSe_2, ACS Nano **13**, 1595 (2019).
[16] T. Ohta, A. Bostwick, T. Seyller, K. Horn, and E. Rotenberg, Controlling the electronic structure of bilayer graphene, Science **313**, 951 (2006).
[17] Y. Zhang, T.-T. Tang, C. Girit, Z. Hao, M. C. Martin, A. Zettl, M. F. Crommie, Y. R. Shen, and F. Wang, Direct observation of a widely tunable bandgap in bilayer graphene, Nature (London) **459**, 820 (2009).
[18] E. McCann and M. Koshino, The electronic properties of bilayer graphene, Rep. Prog. Phys. **76**, 56503 (2013).
[19] A. (Stijn) M. Goossens, S. C. M. Driessen, T. A. Baart, K. Watanabe, T. Taniguchi, and L. M. K. Vandersypen, Gate-defined confinement in bilayer graphene-hexagonal boron nitride hybrid devices, Nano Lett. **12**, 4656 (2012).
[20] M. T. Allen, J. Martin, and A. Yacoby, Gate-defined quantum confinement in suspended bilayer graphene, Nat. Commun. **3**, 934 (2012).
[21] M. Eich, F. Herman, R. Pisoni, H. Overweg, A. Kurzmann, Y. Lee, P. Rickhaus, K. Watanabe, T. Taniguchi, M. Sigrist, T. Ihn, and K. Ensslin, Spin and Valley States in Gate-Defined Bilayer Graphene Quantum Dots, Phys. Rev. X **8**, 031023 (2018).
[22] A. Kurzmann, M. Eich, H. Overweg, M. Mangold, F. Herman, P. Rickhaus, R. Pisoni, Y. Lee, R. Garreis, C. Tong, K. Watanabe, T. Taniguchi, K. Ensslin, and T. Ihn, Excited States in Bilayer Graphene Quantum Dots, Phys. Rev. Lett. **123**, 026803 (2019).
[23] J. Velasco, J. Lee, D. Wong, S. Kahn, H.-Z. Tsai, J. Costello, T. Umeda, T. Taniguchi, K. Watanabe, A. Zettl, F. Wang, and M. F. Crommie, Visualization and control of single-electron charging in bilayer graphene quantum dots, Nano Lett. **18**, 5104 (2018).
[24] Z. Ge, F. Joucken, E. Quezada, D. R. da Costa, J. Davenport, B. Giraldo, T. Taniguchi, K. Watanabe, N. P. Kobayashi, T. Low, and J. Velasco, Visualization and manipulation of bilayer graphene quantum dots with broken rotational symmetry and nontrivial topology, Nano Lett. **20**, 8682 (2020).
[25] Y. Lee, A. Knothe, H. Overweg, M. Eich, C. Gold, A. Kurzmann, V. Klasovika, T. Taniguchi, K. Wantanabe, V. Fal'ko, T. Ihn, K. Ensslin, and P. Rickhaus, Tunable Valley Splitting Due to Topological Orbital Magnetic Moment in Bilayer Graphene Quantum Point Contacts, Phys. Rev. Lett. **124**, 126802 (2020).
[26] M. Reich, *Electrostatically Defined Quantum Dots in Bilayer Graphene* (ETH Zurich, Geneva, 2019).
[27] J. Nilsson and A. H. Castro Neto, Impurities in a Biased Graphene Bilayer, Phys. Rev. Lett. **98**, 126801 (2007).
[28] H. P. Dahal, A. V. Balatsky, and J. X. Zhu, Tuning impurity states in bilayer graphene, Phys. Rev. B **77**, 115114 (2008).
[29] V. V. Mkhitaryan and E. G. Mishchenko, Localized States Due to Expulsion of Resonant Impurity Levels from the Continuum in Bilayer Graphene, Phys. Rev. Lett. **110**, 086805 (2013).

[30] H. P. Ojeda Collado, G. Usaj, and C. A. Balseiro, Impurities and electronic localization in graphene bilayers, Phys. Rev. B **91**, 045435 (2015).
[31] Y. G. Pogorelov, M. C. Santos, and V. M. Loktev, Electric bias control of impurity effects in bilayer graphene, Phys. Rev. B **92**, 075401 (2015).
[32] A. Ferreira, J. Viana-Gomes, J. Nilsson, E. R. Mucciolo, N. M. R. Peres, and A. H. Castro Neto, Castro neto, A. H. unified description of the Dc conductivity of monolayer and bilayer graphene at finite densities based on resonant scatterers, Phys. Rev. B **83**, 165402 (2011).
[33] S. Yuan, H. De Raedt, and M. I. Katsnelson, Electronic transport in disordered bilayer and trilayer graphene, Phys. Rev. B **82**, 235409 (2010).
[34] A. A. Stabile, A. Ferreira, J. Li, N. M. R. Peres, and J. Zhu, Electrically tunable resonant scattering in fluorinated bilayer graphene, Phys. Rev. B **92**, 121411(R) (2015).
[35] J. Katoch, T. Zhu, D. Kochan, S. Singh, J. Fabian, and R. K. Kawakami, Transport Spectroscopy of Sublattice-Resolved Resonant Scattering in Hydrogen-Doped Bilayer Graphene, Phys. Rev. Lett. **121**, 136801 (2018).
[36] F. Joucken, Z. Ge, E. A. Quezada-López, J. L. Davenport, K. Watanabe, T. Taniguchi, and J. Velasco, Determination of the trigonal warping orientation in Bernal-Stacked bilayer graphene via scanning tunneling microscopy, Phys. Rev. B **101**, 161103(R) (2020).
[37] See Supplemental Material at http://link.aps.org/supplemental/10.1103/PhysRevLett.127.106401 for details on the sample fabrication and experimental setup, the method for evaluating the band gap and the electronic doping, and the LDOS calculations. It also presents supplemental experimental data on spatially dependent spectra, the observation of van Hove singularities, as well as theoretical dependence of the dopant-induced states on the electric field and the dopant potential.
[38] P. J. Zomer, S. P. Dash, N. Tombros, and B. J. van Wees, Transfer technique for high mobility graphene devices on commercially available hexagonal boron nitride, Appl. Phys. Lett. **99**, 232104 (2011).
[39] A. M. Goossens, V. E. Calado, A. Barreiro, K. Watanabe, T. Taniguchi, and L. M. K. Vandersypen, Mechanical cleaning of graphene, Appl. Phys. Lett. **100**, 73110 (2012).
[40] I. Horcas, R. Fernández, J. M. Gómez-Rodríguez, J. Colchero, J. Gómez-Herrero, and A. M. Baro, WSXM: A software for scanning probe microscopy and a tool for nanotechnology, Rev. Sci. Instrum. **78**, 13705 (2007).
[41] F. Joucken, C. Bena, Z. Ge, E. A. Quezada-Lopez, S. Pinon, V. Kaladzhyan, T. Tanigushi, K. Watanabe, and J. Velasco, Direct Visualization of Native Defects in Graphite and Their Effect on the Electronic Properties of Bernal-Stacked Bilayer Graphene, arXiv:2104.10620.
[42] P. Lambin, H. Amara, F. Ducastelle, and L. Henrard, Long-range interactions between substitutional nitrogen dopants in graphene: electronic properties calculations, Phys. Rev. B **86**, 045448 (2012).
[43] Y. Tison, J. Lagoute, V. Repain, C. Chacon, Y. Girard, S. Rousset, F. Joucken, D. Sharma, L. Henrard, H. Amara, A. Ghedjatti, and F. Ducastelle, Electronic interaction between nitrogen atoms in doped graphene, ACS Nano **9**, 670 (2015).
[44] Y. Zhang, V. W. Brar, F. Wang, C. Girit, Y. Yayon, M. Panlasigui, A. Zettl, and M. F. Crommie, Giant phonon-induced conductance in scanning tunnelling spectroscopy of gate-tunable graphene, Nat. Phys. **4**, 627 (2008).
[45] N. Néel, C. Steinke, T. O. Wehling, and J. Kröger, Inelastic electron tunneling into graphene nanostructures on a metal surface., Phys. Rev. B **95**, 161410(R) (2017).
[46] M. L. N. Palsgaard, N. P. Andersen, and M. Brandbyge, Unravelling the role of inelastic tunneling into pristine and defected graphene, Phys. Rev. B **91**, 121403(R) (2015).
[47] A. Zabet-Khosousi, L. Zhao, L. Pálová, M. S. Hybertsen, D. R. Reichman, A. N. Pasupathy, and G. W. Flynn, Segregation of sublattice domains in nitrogen-doped graphene, J. Am. Chem. Soc. **136**, 1391 (2014).
[48] F. Joucken, Y. Tison, J. Lagoute, J. Dumont, D. Cabosart, B. Zheng, V. Repain, C. Chacon, Y. Girard, A. R. Botello-Méndez, S. Rousset, R. Sporken, J. C. Charlier, and L. Henrard, Localized state and charge transfer in nitrogen-doped graphene, Phys. Rev. B **85**, 161408(R) (2012).
[49] V. M. Pereira, J. M. B. Lopes dos Santos, and A. H. Castro Neto, Modeling disorder in graphene, Phys. Rev. B **77**, 115109 (2008).
[50] L. Zhao, R. He, K. T. Rim, T. Schiros, K. S. Kim, H. Zhou, C. Gutiérrez, S. P. Chockalingam, C. J. Arguello, L. Pálová, D. Nordlund, M. S. Hybertsen, D. R. Reichman, T. F. Heinz, P. Kim, A. Pinczuk, G. W. Flynn, and A. N. Pasupathy, Visualizing individual nitrogen dopants in monolayer graphene, Science **333**, 999 (2011).
[51] F. Joucken, L. Henrard, and J. Lagoute, Electronic properties of chemically doped graphene, Phys. Rev. Mater. **3**, 110301 (2019).
[52] S.-O. Guillaume, B. Zheng, J.-C. Charlier, and L. Henrard, Electronic properties and STM images of doped bilayer graphene, Phys. Rev. B **85**, 035444 (2012).
[53] M. Telychko, P. Mutombo, M. Ondráček, P. Hapala, F. C. Bocquet, J. Kolorenč, M. Vondráček, P. Jelínek, and M. Švec, Achieving high-quality single-atom nitrogen doping of graphene/SiC(0001) by ion implantation and subsequent thermal stabilization, ACS Nano **8**, 7318 (2014).
[54] E. A. Quezada-Lopez, *Exploring the Graphene/Hexagonal Boron Nitride Heterostructure from the Bottom to the Top* (University of California Santa Cruz, Santa Cruz, 2020).
[55] D. Moldovan, M. Anđelković, and F. Peeters, F. Pybinding v0.9.5: A Python Package for Tight-Binding Calculations (2020), https://doi.org/10.5281/ZENODO.4010216.
[56] A. Weiße, G. Wellein, A. Alvermann, and H. Fehske, The kernel polynomial method, Rev. Mod. Phys. **78**, 275 (2006).
[57] P. Yu and M. Cardona, *Fundamentals of Semiconductors* (Springer-Verlag, Berlin, 2010).
[58] L. Zhao, M. Levendorf, S. Goncher, T. Schiros, L. Pálová, A. Zabet-Khosousi, K. T. Rim, C. Gutiérrez, D. Nordlund, C. Jaye, M. Hybertsen, D. Reichman, G. W. Flynn, J. Park, and A. N. Pasupathy, Local atomic and electronic structure of boron chemical doping in monolayer graphene, Nano Lett. **13**, 4659 (2013).
[59] M. Telychko, P. Mutombo, P. Merino, P. Hapala, M. Ondráček, F. C. Bocquet, J. Sforzini, O. Stetsovych, M. Vondráček, P. Jelínek, and M. Švec, Electronic and chemical properties of donor, acceptor centers in graphene, ACS Nano **9**, 9180 (2015).

[60] P. Willke, J. A. Amani, A. Sinterhauf, S. Thakur, T. Kotzott, T. Druga, S. Weikert, K. Maiti, H. Hofsäss, and M. Wenderoth, Doping of graphene by low-energy ion beam implantation: structural, electronic, and transport properties, Nano Lett. **15**, 5110 (2015).

[61] Y. Wang, V. W. Brar, A. V. Shytov, Q. Wu, W. Regan, H.-Z. Tsai, A. Zettl, L. S. Levitov, and M. F. Crommie, Mapping dirac quasiparticles near a single coulomb impurity on graphene, Nat. Phys. **8**, 653 (2012).

[62] D. Wong, J. Velasco, L. Ju, J. Lee, S. Kahn, H.-Z. Tsai, C. Germany, T. Taniguchi, K. Watanabe, A. Zettl, F. Wang, and M. F. Crommie, Characterization and manipulation of individual defects in insulating hexagonal boron nitride using scanning tunnelling microscopy, Nat. Nanotechnol. **10**, 949 (2015).

[63] L. Ju, L. Wang, T. Cao, T. Taniguchi, K. Watanabe, S. G. Louie, F. Rana, J. Park, J. Hone, F. Wang, and P. L. McEuen, Tunable excitons in bilayer graphene, Science **358**, 907 (2017).